

The oscillatory motion of Jupiter's polar cyclones results from vorticity dynamics

Nimrod Gavriel^{1*} and Yohai Kaspi¹

¹*Department of Earth and Planetary Sciences, Weizmann Institute of Science, Rehovot, Israel*
**nimrod.gavriel@weizmann.ac.il*

Preprint June 8, 2022

Geophys. Res. Lett., 49, 15, (2022). DOI:[10.1029/2022GL098708](https://doi.org/10.1029/2022GL098708)

(Received Mars 22, 2022; Revised June 4, 2022; Accepted June 10, 2022)

Abstract

The polar cyclone at Jupiter's south pole and the 5 cyclones surrounding it oscillate in position and interact. These cyclones, observed since 2016 by NASA's Juno mission, present a unique opportunity to study vortex dynamics and interactions on long time scales. The cyclones' position data, acquired by Juno's JIRAM instrument, is analyzed, showing dominant oscillations with ~ 12 -month periods and amplitudes of ~ 400 km. Here, the mechanism driving these oscillations is revealed by considering vorticity-gradient forces generated by mutual interactions between the cyclones and the latitudinal variation in planetary vorticity. Data-driven estimation of these forces exhibits a high correlation with the measured acceleration of the cyclones. To further test this mechanism, a model is constructed, simulating how cyclones subject to these forces exhibit similar oscillatory motion.

Plain Language Summary

The poles of Jupiter, observed by NASA’s Juno spacecraft since 2016, have a unique symmetric arrangement of storms, where a polar cyclone situated at each pole is surrounded by eight cyclones in the north pole and five cyclones at the south pole. These cyclones, traced for over five years, move with a circular periodic pattern with a 1-year cycle. Here, we explain these periodic patterns by considering the sum of the mutual rejection forces and the polar attraction force resulting from the conservation of momentum inside each cyclone. Using the cyclones’ position data, a calculation of these forces agrees with their measured acceleration, supporting the suggested mechanism. In addition, a simplified model is constructed, which simulates how the south polar cyclones would move under these forces and predict the same type of circular motion.

Key Points:

- The cyclones at Jupiter’s south pole oscillate around their equilibrium positions with a ~ 1 year period and a ~ 400 km amplitude
- A poleward beta-drift force and mutual rejection forces between the cyclones are established as the drivers of the observed oscillations
- The suggested mechanism is supported both by calculations of accelerations and forces based on observations and by an ideal model simulation

1 Introduction

The poles of Jupiter were observed in detail for the first time by the Juno spacecraft in 2016². In contrast with the polar regions of Saturn, which are inhabited by a single polar cyclone (PC)^{3,4}, Jupiter’s PCs are surrounded by a ring of stable circumpolar cyclones (CPCs)^{5,6}. There are 8 CPCs at the north pole and five at the south (Fig. 1), each with a diameter of roughly 5,000 km and velocities reaching 100 ms^{-1} ^{7,8}. Such cyclones can be generated by moist convection^{9,10}, where 2D inverse energy cascade in the turbulent polar regions brings the kinetic energy from the convective scale up to the horizontal scale of the cyclones^{11,12}. These regions are bounded by prograde jets at around latitudes 65°N/S ^{13,14}, which may act as a separating barrier. In contrast with the Great Red Spot, which is centered around latitude 20°S and has a shallow depth (less than 500 km¹⁵) relative to the deep surrounding jets ($\sim 3000 \text{ km}$ ¹⁶), the polar cyclones, subject to the Taylor-Proudman theorem¹⁷ with a vertical axis parallel to the planetary rotation axis and a smaller Rossby number, potentially extend deeper, suggesting a 2D dynamical regime.

The beta-drift is a force that results from a dipole of vorticity (usually termed “beta-gyres”¹⁸) that is induced by an interaction between the tangential velocity of a cyclone and a gradient of potential vorticity (PV) that is present in the background of

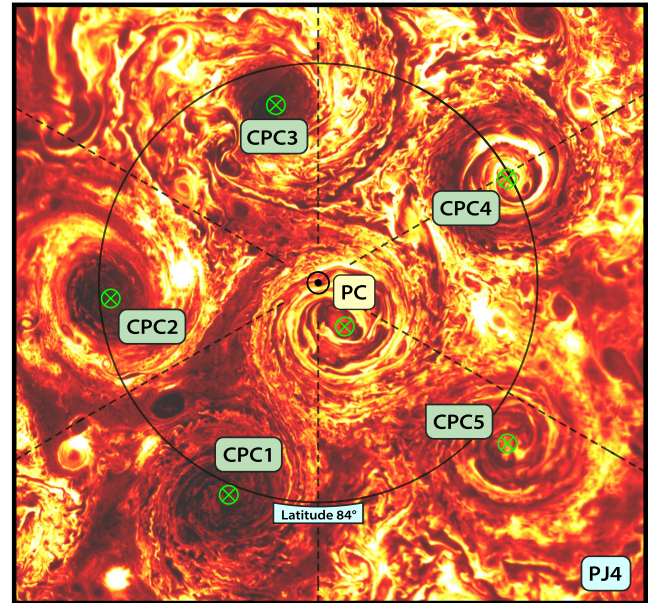


Figure 1: Infrared radiation photograph of Jupiter’s south pole taken by the Jovian Auroral Mapper (JIRAM) instrument on Juno. Image credit: NASA/JPL-Caltech/SwRI/ASI/INAF/JIRAM. The black point represents the pole. The dashed lines represent intervals of 60° longitude (longitude 0° in System III is the line going “upward” from the pole). The green ‘X’s are the estimated location at the centers of the south polar cyclones during PJ4.

the cyclone^{19,20,21}. This force creates a poleward drift on cyclones and an equatorward drift on anticyclones when only the planetary vorticity gradient (β) is considered^{22,20,23}. Beta-drift is a known contributor to the poleward motion of Earth’s tropical cyclones²⁴, and was shown in shallow-water (SW) models to result in cyclones merging into a PC in settings characterizing gas-giants such as Jupiter and Saturn^{25,10,26,27}. Also, vortex crystals^{28,29} similar to Jupiter’s were shown to form around the pole from turbulent initial conditions under the influence of β in quasi-geostrophic (QG) model simulations³⁰. However, other theories for poleward drift of cyclones exist^{31,32}. In addition to β , any PV gradient in the background of a cyclone (e.g., by a jet or a nearby cyclone) can similarly influence its motion^{33,34,35}. For example, the PV gradient due to the zonal mean wind shear and β was shown, using full 3D models, to drive the meridional motion of large vortices on Uranus³⁶ and Neptune³⁷. It was recently found that latitude $\sim 84^\circ$, where the CPCs are observed at both poles of Jupiter, is the latitude where the beta-drift is balanced by an equivalent vorticity-gradient force, in which the source of the PV gradient field is the PC instead of the planetary β ²¹. Such a rejection force between cyclones is dependent on them having an anticyclonic ring around them³⁸, often referred to a ‘vortex shielding’, which is consistent with observations^{8,21,39} and SW simulations of the polar cyclones³⁸. This balance between the forces proved impossible on Saturn, as its

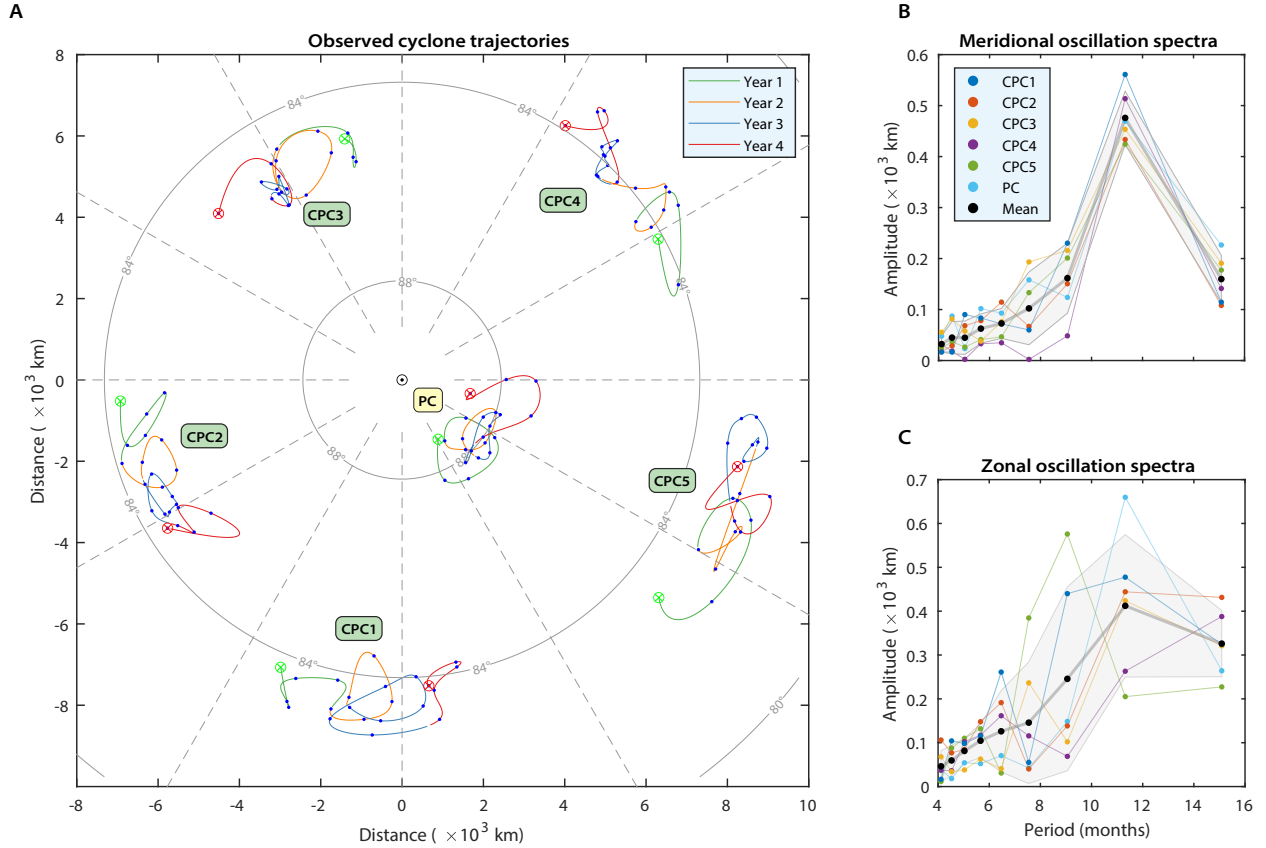


Figure 2: (a) The observed trajectories of the cyclones at the south poles. The green (red) 'X's represent the locations of the cyclones at PJ4 (30), which are the initial (final) locations in the tracked period. For context, see JIRAM's image from PJ4 (Fig. 1). Dots represent observed coordinates¹. The lines are cubic "spline" interpolations between the dots, and are therefore speculative. The lines change their color in the passing of every year since PJ4 (2nd of Feb. 2017). As the data contain less than 4 consecutive years, the red curves only represent 9 months. The black dot represents the pole, gray circles are latitude [$^{\circ}$], and dashed gray lines represent intervals of 30° longitude (longitude 0° in System III is the line going "upward" from the pole). See Movie S1 for an animation of these trajectories. See Fig. S2 for time series of the motion's longitude and latitude. (c,d) The frequency spectra of the observed meridional and zonal (interpolated) motion of the cyclones, respectively. Straight colored lines are linear interpolations between the calculated values (colored dots) and thus do not represent real spectra. Black dots represent the mean spectra between the 6 cyclones, and the gray shade represents a standard deviation (calculated between the 6 cyclones) around the mean. These spectra is presented in terms of oscillation energy in Fig. S1. Notice that the time units presented in this study are Earth's years and months and therefore do not hold physical significance such as orbital periods.

PCs are too large, such that the annulus where they could reject CPCs is too far from the poles, where β dominates, thus inhibiting Saturnian CPCs²¹.

The locations of the CPCs have been monitored since Juno's arrival at Jupiter^{1,7,40}. While the average locations of the cyclones match the calculations of Gavriel and Kaspi (2021)²¹ (hereafter GK21), the individual cyclones were found to oscillate around these stable positions, where perturbations seem to pass on between neighboring cyclones¹. In addition, an average westward drift of approximately 7.5° (3°) per year was measured on the cyclones at the south (north) pole^{7,1}. Here, we extend the work laid out by GK21 and show that in addition to determining the equilibrium conditions of the CPCs, vorticity-gradient forces also control their observed oscillatory motion.

2 Results

Characterizing the Motion of the Cyclones in the Data

To analyze the motion of the PC and the CPCs, we use the data gathered by Juno's JIRAM instrument¹. As the measurements of the cyclones at the north pole were relatively infrequent, we make the analyses only for the south pole. Each orbit of Juno is termed a perijove (PJ), taking ~ 53 days per orbit during the first 30 PJs analyzed in this study. An interpolation of the path that the cyclones went through between PJs is shown in Fig. 2a, where the trajectories of the cyclones are divided by color to the 3 years and 9 months of observations between PJs 4 and 30.

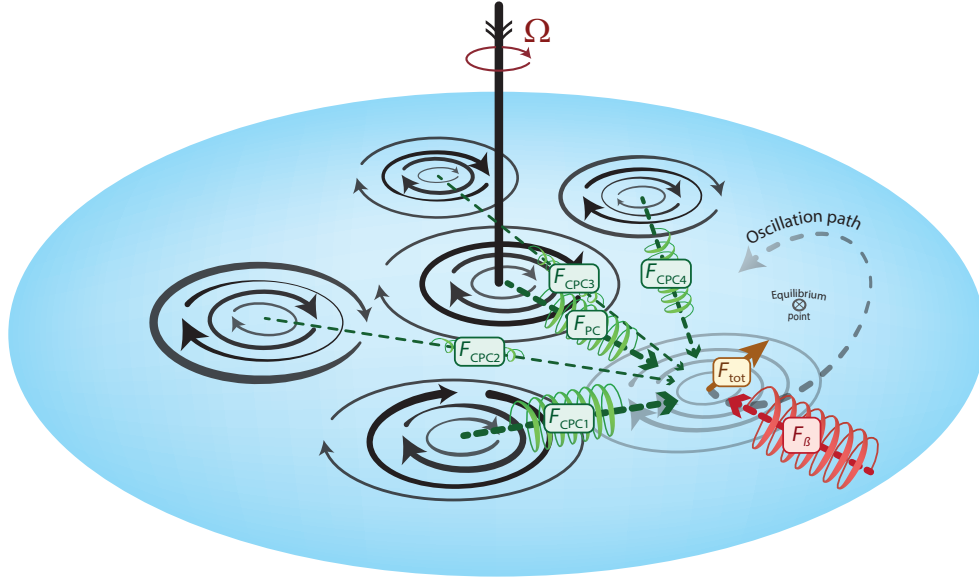


Figure 3: An illustration of the dynamical process driving the observed motion of the south polar cyclones. The thick black line in the center represents the planetary rotation axis and points to the pole. The green arrows and springs represent the rejection forces acting on a CPC due to the vorticity-gradient forces by the individual cyclones. The direction of these forces might rotate by a small factor, as described in section 2.2. The magnitude of the forces (F_{CPCi} by CPC number i , and F_{PC} by the PC), expressed qualitatively by the size of the arrows, decreases with the distance between the cyclones. Therefore, the far CPC2 and CPC3 exert minor rejection on the forced CPC. The red F_{β} represents the polar attraction due to the beta-drift. The blue shade represents the potential magnitude of F_{β} as a function of latitude, which vanishes (white shade) at the pole and gets larger (bluer shades) away from it. The brown arrow (F_{tot}) represents the total net force acting on the cyclone. F_{tot} points towards the equilibrium point, the location where the net force vanishes. The gray dashed arrow illustrates an oscillatory path around the equilibrium point. Due to the motion's inertia, the net force is perpendicular to the path. Note that the portrayed forces are more complex than a linear spring (e.g., they only "push" away from the source and never "pull" toward it), and thus the representation of them as springs is made only for illustrative purposes.

Considering for example CPC2, it can be seen that the motion of the cyclone can be inferred as a circular ~ 1 -year oscillation with an amplitude of $\sim 3^\circ$ longitude (or $\sim 0.3^\circ$ latitude), orbiting an equilibrium point that migrates westward at $\sim 7^\circ$ longitude per year.

We suggest here that this motion results from a dynamical system of 6 bodies (cyclones) with 15 spring-like connections (i.e., rejection forces as described in GK21) between them, in addition to the beta-drift polar attraction acting independently on each cyclone. This picture is illustrated for one cyclone in Fig. 3, where the subject cyclone is rejected by the 5 other cyclones, where each rejection force decreases in magnitude with the distance between the cyclones, and is pushed toward the pole by the beta-drift force (F_{β}). The magnitude of F_{β} increases with distance from the pole²¹. The net force (F_{tot}), resulting from the summation of the 6 forces, deflects the trajectory of the cyclone and results in a circular path concentric to the position of equilibrium. This scheme gets more complicated when taking into account that the 5 rejecting cyclones in Fig. 3 move and oscillate as well, resulting in a more chaotic pattern, which includes various modes between the 6 cyclones. These interferences can be seen in the more complex paths of the 6 cyclones (Fig. 2a). Note that the cumulative trajectory of the cyclones

(Fig. 2a) is not entirely concentric to the pole, but is displaced. This can happen, in the context of the suggested mechanism, if CPCs 2 and 3 "weigh" more than the other cyclones in terms of their rejection forces and their attraction to the pole, thus they get closer poleward while pushing the other cyclones farther away.

To further dissect the observed motion, it is informative to look on the spectra of the observed motion in the meridional and zonal directions (Fig. 2b-c). All of the cyclones have a dominant oscillation mode of a ~ 1 -year period and ~ 400 km amplitude. In the zonal direction (Fig. 2c), the spectrum is more dispersed, perhaps due to the absence of the regulating effect of the beta-drift in the zonal direction, leaving only the complex pattern of rejection forces that change in direction and magnitude with time, thereby creating more variety in the oscillation patterns. For details regarding the data analysis presented in Fig. 2, see Appendix A.

Estimation of the Vorticity-Gradient Forces - Comparison With the Measured Accelerations

To validate that the the observed motion (Fig. 2) results from the hypothesized mechanism laid out in the previous section (Fig.

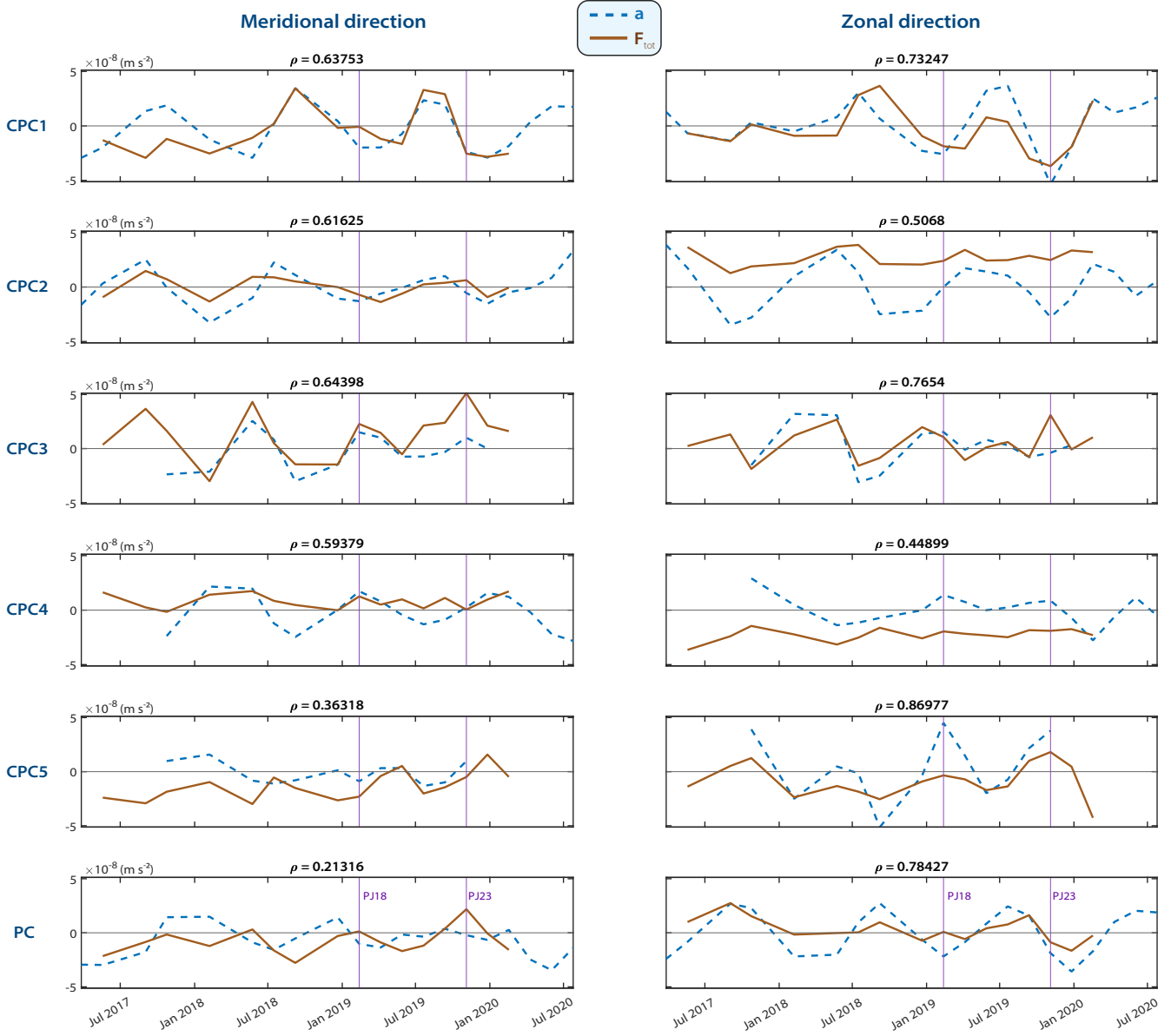


Figure 4: Comparison between the net force and the acceleration of the cyclones, using their instantaneous location data. Each panel represents a time series of the acceleration and force of one cyclone in one direction. Rows represent the different cyclones. The left column is in the meridional direction and the right column is in the zonal direction. The abscissa represents the observation's time. The ordinate, in units of (m s^{-2}) , represents the amplitude of the two curves. The dashed blue curves are the acceleration of the cyclones, calculated by differentiating twice their observed positions with time. The brown lines represent the net force on the cyclones, resulting from the sum of the mutual cyclone rejection forces and F_β (Fig. 3). The solid brown and dashed blue curves are expected to follow each other according to the suggested force balance. The Pearson correlation coefficient (ρ) between these two curves is presented above each panel.

3), it is possible to estimate the net force acting on each cyclone according to its latitude and its distance from the other cyclones at each point in time. From Newton's second law, we expect that the acceleration (\mathbf{a}_i , where i is an index representing the respective cyclone on which the forces are calculated), estimated by differentiating the cyclone's observed position data in time,

should match

$$\mathbf{a}_i = \underbrace{\sum_{j \neq i} \mathbf{F}_{ji} + \mathbf{F}_{\beta i}}_{\mathbf{F}_{\text{tot},i}}, \quad (1)$$

where \mathbf{F}_{ji} is the rejection force vector (per unit mass) by cyclone j , and $\mathbf{F}_{\beta i}$ is the beta-drift force vector (per unit mass).

The forces are ‘‘Rossby forces’’¹⁹, calculated by a concentric integration of the Coriolis force around the cyclone, where the background vorticity alters respectively for each force term (see Appendix A). These calculations require determining 3 global parameters, and 3 characteristic numbers for each of the six cyclones, which dictate their maximum velocity, their size and their morphology. These free parameters are chosen here to stay constant with respect to time, albeit in reality they may also have temporal variations.

To resolve these unknown parameters, an optimization procedure is used to provide the best overall match between the two sides of Eq. 1. For the three cyclone characteristic numbers, up to 20% variability between cyclones was allowed (30% in the case of the morphology factor), relative to mean estimated values. Of the 3 global parameters determined by the optimization algorithm is K_{def} , which is the amount by which the forces are deflected clockwise. This deflection accounts for the fact that after the beta-gyres form, they can be advected by the tangential velocity of the cyclones (clockwise in the case of cyclones in the southern hemisphere) such that the net force is deflected, to some extent, in the clockwise direction⁴¹. In GK21, the analysis of the CPCs latitude of equilibrium assumed a balance between the PC’s rejection force and the beta-effect; here, also taking into account the spatial distribution of the cyclones, we find that rejection of CPCs by CPCs also has a significant component in the meridional direction. The counter balance offered here against this effect, is that turbulence around the pole can partially homogenize the vorticity of the cyclones away from their centers, thereby diminishing their respective gradients and the resulting rejection forces. To take this into account, a factor K_{trb} is applied in the calculation of \mathbf{F}_{ji} . The third global parameter is R_{int} , which determines what fraction of the cyclones’ cores is being integrated to calculate the forces. The values determined for the unknown parameters and all other details of the calculations are elaborated in Appendix A.

The resulting forces, calculated according to the observed instantaneous locations of the cyclones, exhibit a good match with the respective accelerations (Fig. 4). This match is particularly pronounced when looking on CPCs 1 and 3; however, all cases achieve positive correlations (ρ in Fig. 4) that are mostly higher than 0.5. Some mismatch between the curves may be a result of turbulence and impacts of cyclones which arrive at the polar region due to beta-drift and transfer momentum to the 6 cyclones. Such impacts would only directly affect the acceleration of the impacted cyclones, but would not have a signature in the calculation of the forces. To highlight this, two PJs (PJ18⁷, & PJ23¹) when an intruder cyclone was observed in the polar ring are marked by purple lines (Fig. 4), but the impact’s effects may only take place at a specific time during the ~ 3.5 months between the preceding PJ and the following PJ. In the meridional direction of the PC, the relatively low correlation might be expected, as the extremely low β (and therefore \mathbf{F}_β) near the pole leaves it more susceptible to noise. We note here that the acceleration time series presented in Fig. 4, differentiated from the position data, which is spaced ~ 53 days between data

points, only give a measure of the long time-scale accelerations, while instantaneous accelerations can be somewhat different. This is reasonable for the comparison of the vorticity-gradient forces, which only act on long time-scales.

To reassure the reader that the implemented optimization cannot produce this match between acceleration and force out of thin air, we stress that all parameters are constant in time, which means that all the temporal trends in Fig. 4, are direct consequences of the observational data. This implies that without having the underlying physics correct, it is not likely that any set of parameters would be able to produce correlations in the time series, let alone correlate well on the 12 independent cases (Fig. 4). To support this statement, a test with 300 sets of random motion is generated and optimized with the same procedure as was done for Fig. 4, showing very weak correlations between the random accelerations and the resulting forces (see Appendix B, and Fig. S3). Also, the sensitivity of the results (Fig. 4) to variations in the optimized parameters is analysed in Fig. S5. Overall, the match between the forces and the accelerations supports the claim that these vorticity-gradient forces indeed drive the observed motion of the cyclones.

One approach to support the results of Fig. 4 is to analytically estimate the oscillations period from the vorticity-gradient forces. Here, we consider a simple harmonic oscillation of one CPC and two static neighbors in the zonal direction (Fig. S6). Taking a derivative of the mean rejection force per unit mass (F) with a zonal perturbation (x_0) from the position of equilibrium gives the spring constant, from which the oscillation period (T_N) is derived (see full details in Appendix C) as

$$T_N = 2\pi \left(\frac{\partial F}{\partial x_0} \right)^{-\frac{1}{2}}. \quad (2)$$

Estimating Eq. 2 with the values used for Fig. 4 gives $T_N \approx 15$ months, which is relatively close, given the simplicity of the model, to the observed 12-month period. The small overshoot is probably due to the higher complexity of the full 6-body problem. In addition, this analytic analysis predicts how would the oscillations change for different cyclone profiles and for different distances between cyclones (Fig. S7), showing that the oscillations would only be observable for a narrow range of inter-cyclone distances.

Forced-Cyclones Model

To further illustrate how the described mechanism (Fig. 3) results in the observed motion (Fig. 2), a model that simulates the forces and the resulting trajectories of each cyclone with time is constructed. The model advances in time according to

$$\begin{aligned} \frac{\partial \mathbf{u}_i}{\partial t} &= \mathbf{a}_i, \\ \frac{\partial \mathbf{x}_i}{\partial t} &= \mathbf{u}_i, \end{aligned} \quad (3)$$

where t is time, \mathbf{a}_i , \mathbf{u}_i and \mathbf{x}_i are the acceleration (given by Eq. 1), velocity and position vectors of cyclone i , respectively. For initial conditions, we use the observed locations of the cyclones

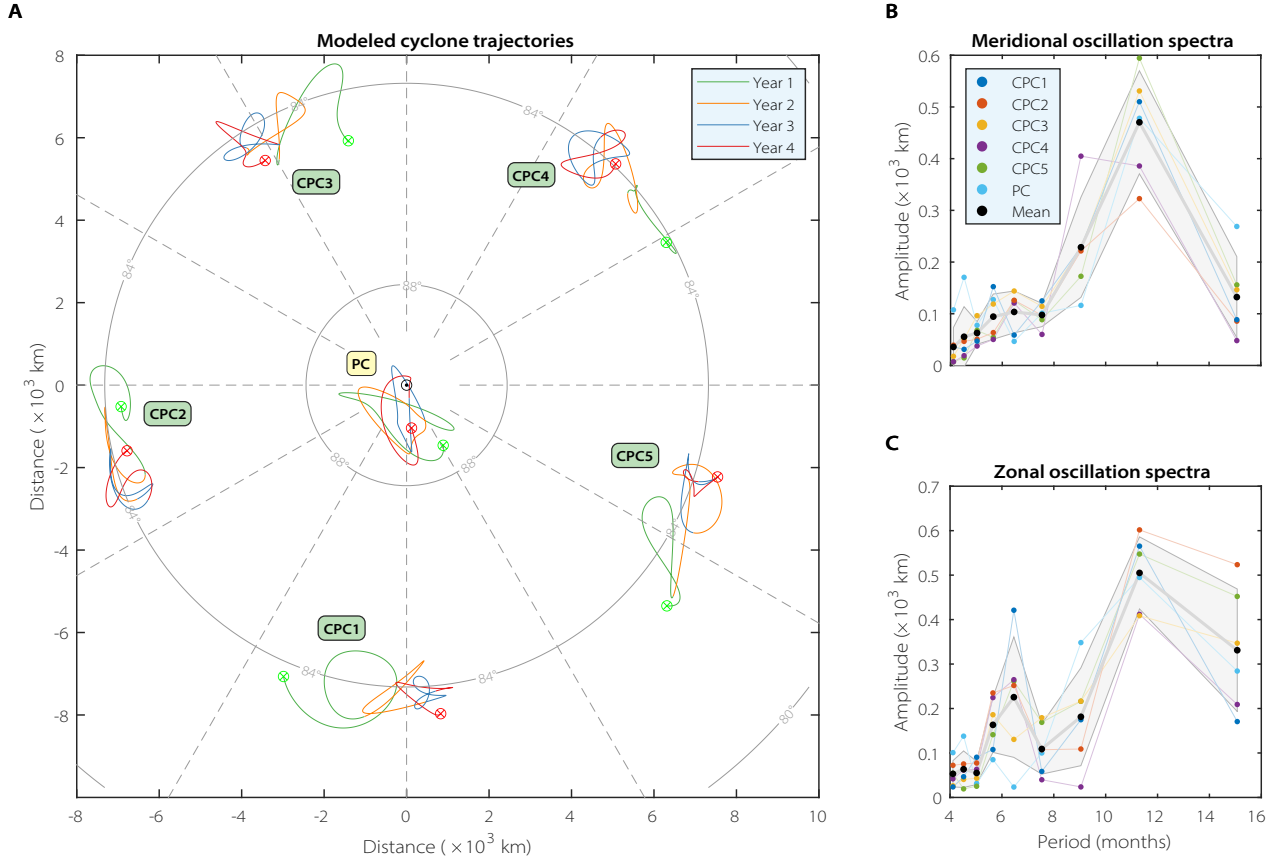


Figure 5: The modelled trajectories and spectra of Jupiter’s south polar cyclones. (a) The trajectories of the modeled cyclones, moving in time according to Eq. 1 and Eq. 3. The green ‘X’ denote the initial position of each cyclone, corresponding to the observed positions at PJ4. The red ‘X’ are the simulated final positions at PJ30. The trends change color after each year of simulation. An animation of the simulation is available in the SI (Movie S2). (b,c) Zonal and meridional modelled oscillation spectra, respectively. The black dots and gray shades represent the mean and the 1 STD range around it, respectively, calculated for each period between the 6 cyclones. These spectra is presented in terms of oscillation energy in Fig. S8.

at PJ4 (green crosses in Fig. 2a), and for initial velocity we differentiate with time the locations during the first two observations. To find the unknown parameters, as described in the previous section, another optimization is performed, this time to get the simulated trajectories and spectra (Fig. 5) as close as possible to the observations (Fig. 2). The final values determined for these parameters and all other details of the model are described in Appendix D.

As the model has no dissipation of energy, it is susceptible to resonances. However, dissipating the energy would mean that without also inserting energy, the motion would cease. To insert energy would require forcing the cyclones with artificial frequencies and amplitudes, thus biasing the model results. The optimization procedure, on the other hand, manages to avoid resonance by fine-tuning of the parameters, without insertion of additional terms to the forces balance. For this, the model cannot use the parameter values used for Fig. 4, as it results in a resonant mode. Alternatively, using the model set for the analysis of Fig. 4 shows good correlations, but the magnitudes have mismatches between the forces and the accelerations. Never-

theless, the differences between the final parameter sets of the two analyses (Fig. 4 and Fig. 5) are relatively small, where both sets are within a reasonable physical range (see Table S1).

The model results (Fig. 5) capture properly the observed motion patterns of the south polar cyclones (Fig. 2). These patterns include both the form of their trajectories and the motion’s spectra, which peak near 12 months with amplitudes of ~ 400 kilometers. These model results exemplify that the mechanism described in this study (Fig. 3) can, in fact, result in the observed motion. The similarity between the model and the observations adds additional support that the theory outlined in GK21 and here, can explain the transient motion of Jupiter’s PCs and CPCs, in addition to describing their equilibrium states.

3 Discussion

By showing that vorticity gradients, induced both by the polar cyclones and by β , control the leading order balance of both the statistic steady-state²¹ and the dynamic motion of the polar

cyclones (Fig. 4), we surmise that Jupiter’s polar flow regime is largely barotropic, when looking at the scale of the cyclones (scales bigger than ~ 500 km). This implies on the cyclones’ depth, where either the thin shallow-water equations, indicating on shallow cyclones, or deep 2D framework can capture the cyclone’s motion. If the cyclones are indeed barotropic and deep, in agreement with the Taylor-Proudman theorem, they would extend uninterruptedly down to the semi-conducting region, where they would stop spinning due to magnetic drag^{42,43,44,45}. In this case, heat convection from Jupiter’s core would be a plausible energy source for the cyclones^{46,47,48,49}. These two options should come to mind when trying to analyze how the cyclones were formed, how they are maintained, and what determines their strength and morphology.

The north pole of Jupiter is expected to demonstrate similar dynamics for its cyclones as highlighted in this study for the south pole. However, as the available infrequent data do not allow a similar detailed analysis, this test is left for future studies, when more data might be gathered. For the south pole, while matching the cyclone’s acceleration and position-based forces (Fig. 4) required resolving unknown coefficients with an optimization procedure, the high correlations between them were found to be a robust feature, regardless of the determined values (within a sensible range, see Fig. S5). For the robustness of the model simulation, unoptimized runs with simple assumptions and identical 6 cyclones also produce oscillation patterns similar to the observations (Fig. S9). Overall, the results of both observational analysis (Figs. 4) and of an idealized time-evolution model (Fig. 5), establish the role of vorticity-gradient forces (Fig. 3) as the driving mechanism of the Jovian south polar cyclones’ observed motion (Fig. 2), and highlight the importance of considering these forces in future studies on gas giants’ polar dynamics and vortex motions at large.

Open Research

No new data sets were generated during the current study. The data analysed in this study were published by Mure et al. (2021)¹ (DOI: <https://doi.org/10.1029/2021GL094235>), as cited in the text. The figure files and Matlab scripts are available at: <https://doi.org/10.5281/zenodo.6611745>.

Acknowledgements

This research has been supported by the Minerva Foundation with funding from the Federal German Ministry for Education and Research and the Helen Kimmel Center for Planetary Science at the Weizmann Institute of Science.

Competing Interests

Authors declare that they have no competing interests.

References

1. Mura, A. *et al.* Oscillations and stability of the Jupiter polar cyclones. *Geophys. Res. Lett.* **48**, e2021GL094235 (2021).
2. Bolton, S. J. *et al.* Jupiter’s interior and deep atmosphere: The initial pole-to-pole passes with the Juno spacecraft. *Science* **356**, 821–825 (2017).
3. Sánchez-Lavega, A., Hueso, R., Pérez-Hoyos, S. & Rojas, J. A strong vortex in Saturn’s south pole. *Icarus* **184**, 524–531 (2006).
4. Baines, K. H. *et al.* Saturn’s north polar cyclone and hexagon at depth revealed by Cassini/VIMS. *Planet. Space Sci.* **57**, 1671–1681 (2009).
5. Orton, G. S. *et al.* The first close-up images of Jupiter’s polar regions: Results from the Juno mission JunoCam instrument. *Geophys. Res. Lett.* **44**, 4599–4606 (2017).
6. Adriani, A. *et al.* Clusters of cyclones encircling Jupiter’s poles. *Nature* **555**, 216–219 (2018).
7. Adriani, A. *et al.* Two-year observations of the Jupiter polar regions by JIRAM on board Juno. *J. Geophys. Res. (Planets)* e2019JE006098 (2020).
8. Grassi, D. *et al.* First estimate of wind fields in the Jupiter polar regions from JIRAM-Juno images. *J. Geophys. Res. (Planets)* **123**, 1511–1524 (2018).
9. O’Neill, M. E., Emanuel, K. A. & Flierl, G. R. Polar vortex formation in giant-planet atmospheres due to moist convection. *Nature Geoscience* **8**, 523–526 (2015).
10. O’Neill, M. E., Emanuel, K. A. & Flierl, G. R. Weak jets and strong cyclones: Shallow-water modeling of giant planet polar caps. *J. Atmos. Sci.* **73**, 1841–1855 (2016).
11. Moriconi, M. *et al.* Turbulence power spectra in regions surrounding Jupiter’s south polar cyclones from Juno/JIRAM. *J. Geophys. Res. (Planets)* **125**, e2019JE006096 (2020).
12. Siegelman, L. *et al.* Moist convection drives an upscale energy transfer at Jovian high latitudes. *Nature Physics* **1–5** (2022).
13. Rogers, J. *et al.* Flow patterns of Jupiter’s south polar region. *Icarus* **372**, 114742 (2022).
14. Rogers, J., Adamoli, G., Jacquesson, M., Vedovato, M. & Mettig, H. Jupiter’s high northern latitudes: patterns and dynamics of the N3 to N6 domains. *JUPOS & BAA* (2017).
15. Parisi, M. *et al.* The depth of Jupiter’s Great Red Spot constrained by Juno gravity overflights. *Science* **374**, 964–968 (2021).
16. Kaspi, Y. *et al.* Jupiter’s atmospheric jet streams extend thousands of kilometres deep. *Nature* **555**, 223–226 (2018).
17. Vallis, G. K. *Atmospheric and oceanic fluid dynamics* (Cambridge University Press, 2017).
18. Sutyrin, G. G. & Flierl, G. R. Intense vortex motion on the beta plane: Development of the beta gyres. *J. Atmos. Sci.* **51**, 773–790 (1994).
19. Rossby, C. On displacements and intensity changes of atmospheric vortices. *J. Mar. Res.* **7**, 71 (1948).

20. Chan, J. C. The physics of tropical cyclone motion. *Ann. Rev. Fluid Mech.* **37**, 99–128 (2005).
21. Gavriel, N. & Kaspi, Y. The number and location of Jupiter’s circumpolar cyclones explained by vorticity dynamics. *Nature Geoscience* **14**, 559–563 (2021).
22. Franklin, J. L., Feuer, S. E., Kaplan, J. & Aberson, S. D. Tropical cyclone motion and surrounding flow relationships: Searching for beta gyres in omega dropwindsonde datasets. *Mon. Weath. Rev.* **124**, 64–84 (1996).
23. Merlis, T. M. & Held, I. M. Aquaplanet simulations of tropical cyclones. *Curr. Clim. Change Rep.* **5**, 185–195 (2019).
24. Zhao, H., Wu, L. & Zhou, W. Observational relationship of climatologic beta drift with large-scale environmental flows. *Geophys. Res. Lett.* **36** (2009).
25. Scott, R. Polar accumulation of cyclonic vorticity. *Geophys. Astrophys. Fluid Dyn.* **105**, 409–420 (2011).
26. Brueshaber, S. R., Sayanagi, K. M. & Dowling, T. E. Dynamical regimes of giant planet polar vortices. *Icarus* **323**, 46–61 (2019).
27. Brueshaber, S. R. & Sayanagi, K. M. Effects of forcing scale and intensity on the emergence and maintenance of polar vortices on Saturn and Ice Giants. *Icarus* **361**, 114386 (2021).
28. Fine, K., Cass, A., Flynn, W. & Driscoll, C. Relaxation of 2D turbulence to vortex crystals. *Phys. Rev. Lett.* **75**, 3277 (1995).
29. Schecter, D., Dubin, D., Fine, K. & Driscoll, C. Vortex crystals from 2D Euler flow: Experiment and simulation. *Phys. of Fluids*. **11**, 905–914 (1999).
30. Siegelman, L., Young, W. R. & Ingersoll, A. P. Polar vortex crystals: Emergence and structure. *Proc. Natl. Acad. Sci. U.S.A.* **119**, e2120486119 (2022).
31. Afanasyev, Y. & Zhang, Y. Cyclonic circulation of Saturn’s atmosphere due to tilted convection. *Nature Geoscience* **11**, 164–167 (2018).
32. Afanasyev, Y. & Huang, Y.-C. Poleward translation of vortices due to deep thermal convection on a rotating planet. *Geophys. Astrophys. Fluid Dyn.* **114**, 821–834 (2020).
33. Chan, J. & Law, A. The interaction of binary vortices in a barotropic model. *Meteorol. Atmos. Phys.* **56**, 135–155 (1995).
34. Shin, S.-E., Han, J.-Y. & Baik, J.-J. On the critical separation distance of binary vortices in a nondivergent barotropic atmosphere. *J. Meteorol. Soc. Jpn.* **84**, 853–869 (2006).
35. Rivière, G., Arbogast, P., Lapeyre, G. & Maynard, K. A potential vorticity perspective on the motion of a mid-latitude winter storm. *Geophys. Res. Lett.* **39**, 12808 (2012).
36. LeBeau, R., Farmer, K., Sankar, R., Hadland, N. & Palotai, C. A Numerical investigation of the Berg feature on Uranus as a vortex-driven system. *Atmosphere* **11**, 52 (2020).
37. LeBeau, R. & Dowling, T. EPIC simulations of time-dependent, three-dimensional vortices with application to Neptune’s Great Dark Spot. *Icarus* **132**, 239–265 (1998).
38. Li, C., Ingersoll, A. P., Klipfel, A. P. & Brettle, H. Modeling the stability of polygonal patterns of vortices at the poles of Jupiter as revealed by the Juno spacecraft. *Proc. Natl. Acad. Sci. U.S.A.* **117**, 24082–24087 (2020).
39. Ingersoll, A. *et al.* Polygonal patterns of cyclones on Jupiter: Convective forcing and anticyclonic shielding. *Research Square - Preprint* (2021).
40. Tabataba-Vakili, F. *et al.* Long-term tracking of circumpolar cyclones on Jupiter from polar observations with Juno-Cam. *Icarus* **335**, 113405 (2020).
41. Fiorino, M. & Elsberry, R. L. Some aspects of vortex structure related to tropical cyclone motion. *J. Atmos. Sci.* **46**, 975–990 (1989).
42. Liu, J., Goldreich, P. M. & Stevenson, D. J. Constraints on deep-seated zonal winds inside Jupiter and Saturn. *Icarus* **196**, 653–664 (2008).
43. Dietrich, W. & Jones, C. A. Anelastic spherical dynamos with radially variable electrical conductivity. *Icarus* **305**, 15–32 (2018).
44. Duer, K., Galanti, E. & Kaspi, Y. Analysis of Jupiter’s deep jets combining Juno gravity and time-varying magnetic field measurements. *Astrophys. J. Lett.* **879**, L22 (2019).
45. Kaspi, Y. *et al.* Comparison of the deep atmospheric dynamics of Jupiter and Saturn in light of the Juno and Cassini gravity measurements. *Space Sci. Rev.* **216**, 5, 84, 1–27 (2020).
46. Yadav, R. K., Heimpel, M. & Bloxham, J. Deep convection-driven vortex formation on Jupiter and Saturn. *Sci. Adv.* **6**, eabb9298 (2020).
47. Yadav, R. K. & Bloxham, J. Deep rotating convection generates the polar hexagon on Saturn. *Proc. Natl. Acad. Sci. U.S.A.* **117**, 13991–13996 (2020).
48. Garcia, F., Chambers, F. R. & Watts, A. L. Deep model simulation of polar vortices in gas giant atmospheres. *Mon. Not. Roy. Astro. Soc.* **499**, 4698–4715 (2020).
49. Cai, T., Chan, K. L. & Mayr, H. G. Deep, Closely Packed, Long-lived Cyclones on Jupiter’s Poles. *Planet. Sci. J.* **2**, 81 (2021).
50. Chan, J. C. & Williams, R. Analytical and numerical studies of the beta-effect in tropical cyclone motion. Part I: Zero mean flow. *J. Atmos. Sci.* **44**, 1257–1265 (1987).

Supplementary Information

Movie S1. (Link) An animation of the observed trajectories of the south polar cyclones, as illustrated in Fig. 2a, along the 45-months of observations. The blue arrows represent the estimated net forces on the cyclones, as presented in Fig. 4.

Movie S2. (Link) An animation of the simulated trajectories of the south polar cyclones, as illustrated in Fig. 5a, along 45-months. The blue arrows represent the net forces on the cyclones.

A Data analysis methods

Trajectories and spectra

In this subsection the procedures done for creating Fig. 2 are elaborated. In this study we used the data acquired by the Jovian Infrared Auroral Mapper (JIRAM) and published in¹. Specifically, the used data for the observed locations of the south polar cyclones per PJ is listed in Table 1 of¹. Here, this data was converted to Cartesian coordinates (x, y) via the transformation

$$x = -R_J \cos \theta \sin \lambda, \quad y = R_J \cos \theta \cos \lambda, \quad (4)$$

where R_J is the mean radius of Jupiter ($= 69,911$ km), θ is latitude and λ is longitude. The Cartesian data was interpolated for the periods between PJs using a cubic “spline” interpolation. This interpolated data is plotted as solid lines in Fig. 2, where the dots represent the actual published data. The trajectories can also be presented as a time series of latitude and longitude (Fig. S2), emphasizing the dominance of the 12-month period oscillations.

For plotting Fig. 2b-c, the interpolated data is first transformed back to latitude and longitude by

$$\theta = \cos^{-1} \left(\frac{\sqrt{x^2 + y^2}}{R_J} \right), \quad \lambda = \tan^{-1} \left(\frac{y}{x} \right) - \frac{\pi}{2}, \quad (5)$$

to evaluate the cumulative zonal (L_λ) and meridional (L_θ) distances traveled by a cyclone i at time step k as

$$\begin{aligned} L_{\lambda(i,k)} &= L_{\lambda(i,k-1)} + R_J \cos(\theta_{i,k}) (\lambda_{i,k} - \lambda_{i,k-1}), \\ L_{\theta(i,k)} &= L_{\theta(i,k-1)} + R_J \cos(\theta_{i,k} - \theta_{i,k-1}), \end{aligned} \quad (6)$$

where we define $L_{\lambda(i,1)} = L_{\theta(i,1)} = 0$. Then, after removing the mean and linear trends, a fast Fourier transform (FFT) was performed on the time series defined by Eq. 6. This calculation produces the oscillation amplitudes, $A_{i,n}(T/n)$, where T is the duration of the time series (~ 45 months) and n is a natural number. As the analyzed location data are 53 days apart, only oscillation periods larger than 4 months are displayed (Fig. 2b-c), thus not regarding calculated spectra that are artifacts of the interpolation method. Similarly, the displayed spectra is limited to oscillation periods smaller than 16 months, as higher periods are calculated based on less than three occurrences in the available data set, and are thus statistically insignificant. The black dots in Fig. 2b-c represent the mean (between cyclones) spectra,

$$\overline{A_n} = \frac{1}{6} \sum_{i=1}^6 A_{i,n}, \quad (7)$$

and the black shades frame the area

$$\overline{A_n} \pm \sqrt{\text{Var}(A_{1,n}, A_{2,n}, A_{3,n}, A_{4,n}, A_{5,n}, A_{6,n})}, \quad (8)$$

representing the standard error around the mean. In Fig. S1, the spectra is presented in terms of energy instead of metric amplitudes.

Estimating the forces acting on the cyclones and their acceleration

To illustrate how the forces illustrated in Fig. 3 result in the observed oscillatory motion (Fig. 2), these forces are estimated according to the following layout.

Velocity profile for each cyclone

The ideal tangential velocity profile ($U_i(r_i)$, where r_i is the distance from the cyclone’s center) around a cyclone i , where i is the cyclone’s identifier (ranging from 1 to 6 in the SH), used in this study is⁵⁰

$$U_i(r_i) = V_i \left(\frac{r_i}{R_i} \right) \exp \left[\frac{1}{b_i} \left(1 - \left(\frac{r_i}{R_i} \right)^{b_i} \right) \right], \quad (9)$$

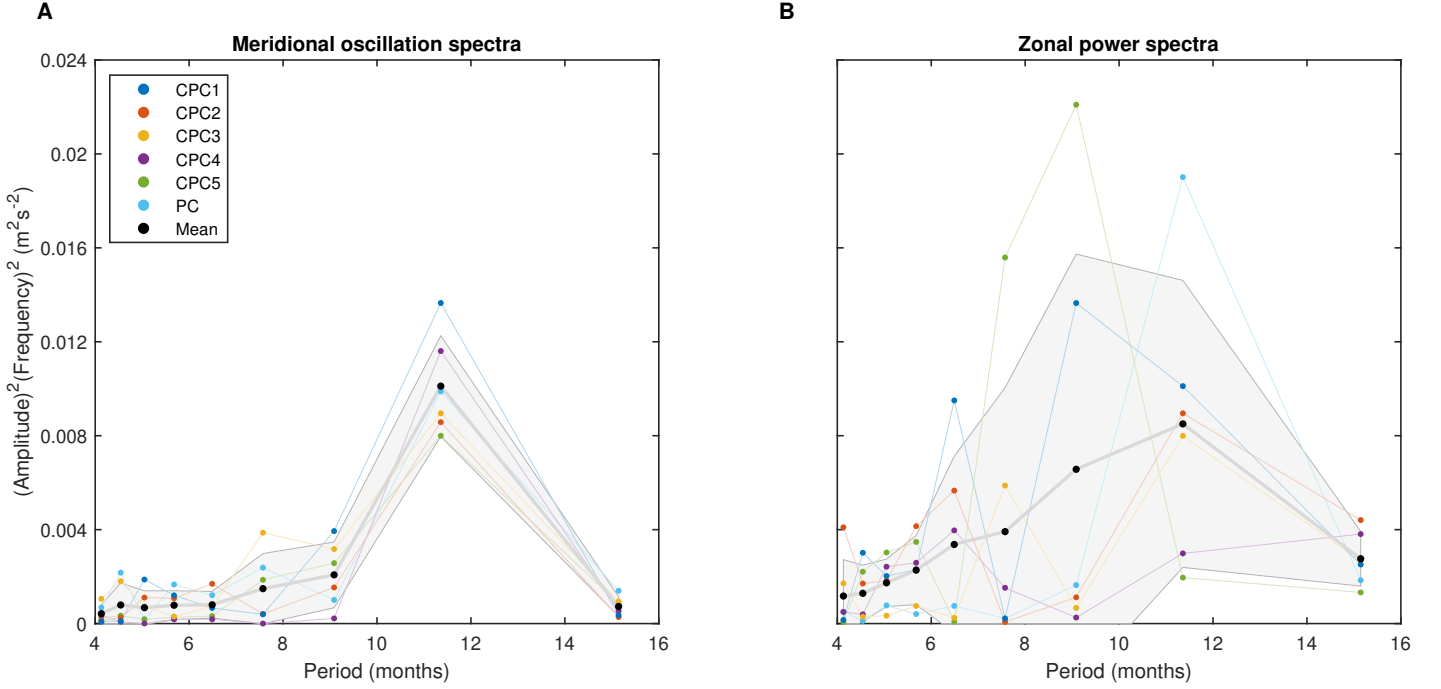


Figure S1: Energy spectra of the observed motion. Here, panels a-b are the same as Fig. 2 panels b and c, but here the ordinate represents the energy of the oscillations (amplitude² frequency²) rather than just the amplitude (A_n).

where V_i , R_i and b_i are the maximum velocity, the radius of maximum velocity and a steepness constant of cyclone i , respectively. This ideal profile captures the observed trends of an inner solid-rotating core and an exponential decay outside, while the connection between the two regions is continuous. The distance, r_i , from cyclone i , and the angle ϕ_i are calculated as

$$\begin{aligned} r_i(x, y, t) &= \sqrt{(x - x_i(t))^2 + (y - y_i(t))^2}, \\ \phi_i(x, y, t) &= \tan^{-1} \left(\frac{y - y_i(t)}{x - x_i(t)} \right), \end{aligned} \quad (10)$$

where $x_i(t)$ and $y_i(t)$, are the instantaneous coordinates of the center of cyclone i at time t in the x and y directions. The Cartesian velocities in the x and y directions are thus

$$\begin{aligned} u_i(r_i, \phi_i) &= -U_i(r_i) \sin(\phi_i), \text{ and} \\ v_i(r_i, \phi_i) &= U_i(r_i) \cos(\phi_i), \end{aligned} \quad (11)$$

respectively.

Potential vorticity

Using Eqs. 9-11, the relative vorticity field due to the velocity profile of cyclone i , calculated as $\xi_i = \frac{1}{r_i} \frac{\partial}{\partial r_i} (r_i U_i)$, is

$$\xi_i(r_i) = \frac{V_i}{R_i} \left(2 - \left(\frac{r_i}{R_i} \right)^{b_i} \right) \exp \left[\frac{1}{b_i} \left(1 - \left(\frac{r_i}{R_i} \right)^{b_i} \right) \right]. \quad (12)$$

The planetary vorticity is

$$f = 2\Omega \cos \left(\frac{\sqrt{x^2 + y^2}}{R_J} \right), \quad (13)$$

where Ω and R_J are the rotation rate and mean radius of Jupiter, respectively.

Calculating the forces

The individual forces are calculated as the net mean integrated Coriolis forces (sometimes referred to as a 'Rossby force',¹⁹) resulting from the interaction of the tangential velocity of the forced cyclone with either f , representing the beta-drift force, or the relative

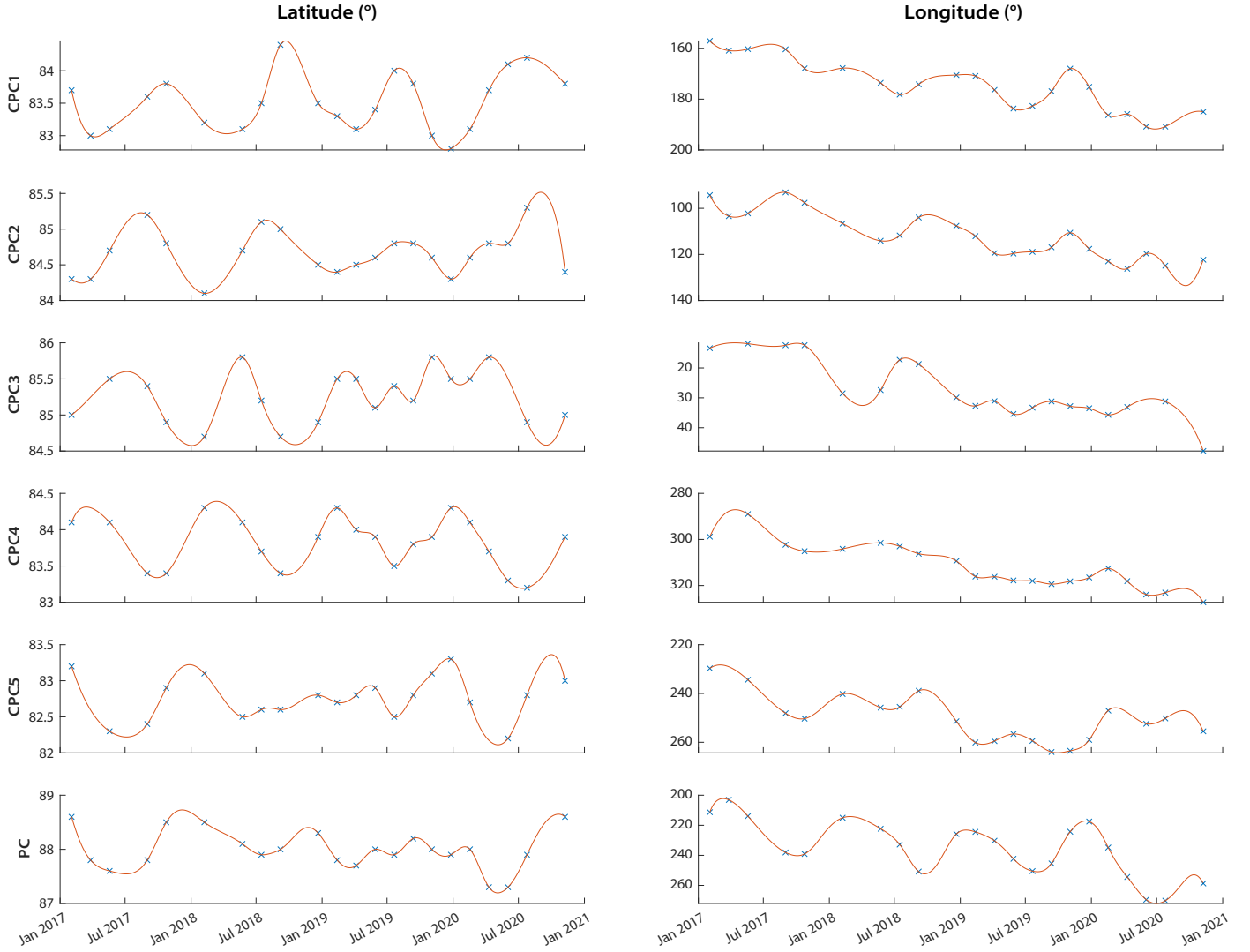


Figure S2: Time series of the observed zonal and meridional motion of Jupiter's south polar cyclones. Here, the blue 'X's represent the observed values, while the red lines represent the interpolations between the observations (the same interpolations as presented in Fig. 2). The longitude time series were previously plotted in Mura2021 (their Fig. 2).

vorticity of the other cyclones, representing the mutual rejection forces between the cyclones. The forces would be calculated in two parts. First, the forces (per unit mass) in the x and y directions are integrated as

$$\begin{aligned} \tilde{F}_{\beta i,x} &= \left(\iint dS_i \right)^{-1} \iint f v_i dS_i, & \tilde{F}_{\beta i,y} &= - \left(\iint dS_i \right)^{-1} \iint f u_i dS_i, \\ \tilde{F}_{ji,x} &= \left(\iint dS_i \right)^{-1} \iint K_{\text{trb}} \xi_j v_i dS_i, & \tilde{F}_{ji,y} &= - \left(\iint dS_i \right)^{-1} \iint K_{\text{trb}} \xi_j u_i dS_i, \end{aligned} \quad (14)$$

where ξ_j is evaluated at r_j for cyclones $j \neq i$, and K_{trb} is a global constant that parameterizes turbulence in the atmosphere, which can mix and diminish the PV of each cyclone, when integrated far from its core, around a neighbor forced cyclone. The integrated area $dS_i = r_i dr_i d\phi_i$, is in the range $\phi_i = [0, 2\pi]$ and $r_i = [0, R_{\text{int}}]$, where R_{int} is a global constant that defines what fraction of the cyclone's core is numerically integrated.

Advection of vorticity anomalies with the tangential velocity of a cyclone can result in a westward component to the planetary beta-drift force^{41,20}. Therefore, a clockwise (in the direction of the rotation of SH cyclones) deflection of the forces is allowed. This results in the forces having the final form

$$\begin{aligned} F_{\beta i,x} &= \tilde{F}_{\beta i,x} (1 - K_{\text{def}}) + \tilde{F}_{\beta i,y} K_{\text{def}}, & F_{\beta i,y} &= \tilde{F}_{\beta i,y} (1 - K_{\text{def}}) - \tilde{F}_{\beta i,x} K_{\text{def}}, \\ F_{ji,x} &= \tilde{F}_{ji,x} (1 - K_{\text{def}}) + \tilde{F}_{ji,y} K_{\text{def}}, & F_{ji,y} &= \tilde{F}_{ji,y} (1 - K_{\text{def}}) - \tilde{F}_{ji,x} K_{\text{def}}, \end{aligned} \quad (15)$$

Table S1: Parameter sets determined for Fig. 4 (Set 1), Fig. 5 (Set 2), and the mean and variance between them. The variances of the per-cyclone parameters (V_i, R_i, b_i) are between the combined 12 numbers of both sets. ρ_{mean} is the correlation between the observed acceleration and the net force calculated with the respective set, averaged for the 6 cyclones and the 2 directions. Set 3 is the result of optimization with only 2 variables (Fig. S4). The ideal case lists the values determined for the model robustness tests (Section S3)

	K_{def}	K_{trb}	R_{int}	V_1 V_2 V_3 (ms^{-1}) V_4 V_5 V_6	R_1 R_2 R_3 (km) R_4 R_5 R_6	b_1 b_2 b_3 b_4 b_5 b_6	ρ_{mean}
Set 1	0.1889	0.3176	0.0643	92.7 78.01 86.19 87.17 79.17 82.22	1,192 1,031 1,115 1,031 1,060 1,069	0.678 0.893 0.748 1.028 0.632 0.817	0.598
Set 2	0.1148	0.3128	0.1041	79.68 86.11 89.34 85.63 81.74 84.98	1,042 1,134 1,112 1,093 1,051 1,145	0.702 0.743 0.799 0.821 0.832 0.730	0.622
Mean	0.1519	0.3152	0.0842	84.41	1,090	0.7852	
STD	0.0524	0.0034	0.0281	4.3816	51	0.1059	
STD (%)	34.5%	1.1%	33.4%	5.2%	4.7%	13.5%	
Set 3	0	0.2768	0.0472	85	1,100	0.78	0.536
Ideal	0	1	0.1	85	1,100	0.78	0.4179

where $0 \leq K_{\text{def}} \leq 1$ is a global constant determining the magnitude of the clockwise deflection. The net force vector is finally

$$\mathbf{F}_{\text{tot},i} = \mathbf{F}_{\beta,i} + \sum_{j \neq i} \mathbf{F}_{j,i}, \quad (16)$$

where the x and y components of the force vectors are defined by Eqs. 14-15.

Finding the unknown parameters

The theory outlined in this manuscript suggests that $\mathbf{F}_{\text{tot},i}$, an idealized parameterization for the force density acting on each cyclone according to the latitude of the cyclone ($\mathbf{F}_{\beta,i}$) and the distance to all the other cyclones ($\mathbf{F}_{j,i}$), should be equal to the acceleration of the same cyclone, according to Newton's second law. The acceleration, \mathbf{a}_i , is estimated from the position data using finite difference derivative approximations in the x and y directions on the observed locations time-series. To estimate $\mathbf{F}_{\text{tot},i}$, unknown parameters should be determined. These parameters include three global constants: K_{def} , K_{trb} and R_{int} , and 3 sets of individual constants for the six cyclones: V_i , R_i and b_i , which, for simplicity, are assumed here to remain constant during the 4-year time series. To determine these parameters, an optimization procedure is executed, which searches for a set that minimizes a cost function containing 4 additive parts of equal weight: (i) 1 minus the mean correlation between $\mathbf{F}_{\text{tot},i}$ and \mathbf{a}_i ; (ii) the differences between the time series of $\mathbf{F}_{\text{tot},i}$ and \mathbf{a}_i , averaged for all 6 cyclones; (iii) The difference between the maximum positive amplitudes of $\mathbf{F}_{\text{tot},i}$ and \mathbf{a}_i ; (iv) The difference between the maximum negative amplitudes of $\mathbf{F}_{\text{tot},i}$ and \mathbf{a}_i . The optimization was executed using Matlab's `fmincon` function, which uses the 'interior-point' algorithm. The resulting set, used for plotting Fig. 4, is displayed in Table. S1 under "Set 1".

B Robustness and sensitivity of the correlation analysis to optimization

In this section we verify that the optimization procedure cannot find the same level of correlation in random data as it can find in the real data. Afterwards, we check the sensitivity of the results to the chosen values determined by the optimization. We begin this analysis by generating 300 sets of random data. Each set is composed of a random trajectory time series (with the total period, ~ 4 years, of the real data) for each of the six cyclones. The initial positions for each random set are the positions of the six cyclones at PJ4. As the vorticity-gradient forces (Eq. 16) are functions of the cyclones' positions, the way to verify that the optimization cannot

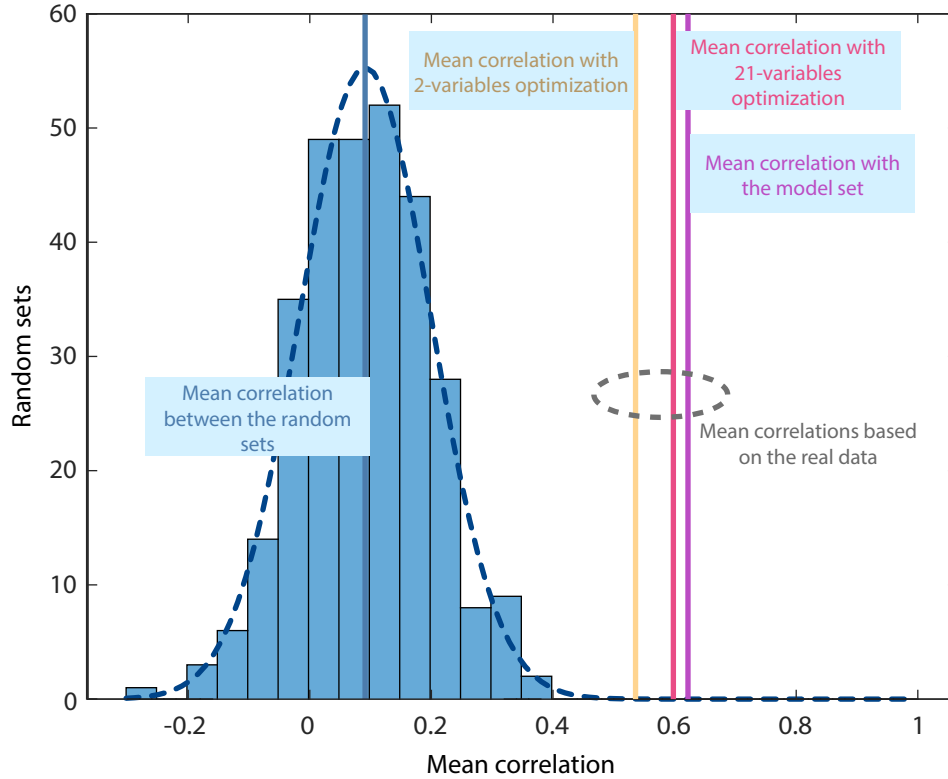


Figure S3: Histogram of the random acceleration sets results. The histogram presents the mean correlations (abscissa) where the total amount of sets is 300. The vertical blue line represents the mean of the 300 mean correlations. The dashed line represents the Gaussian distribution of the mean correlations between the 300 sets. The vertical red line represents the mean correlation of Set 1 (Tab. S1). The yellow vertical line represents the mean correlation of Set 3, found by optimizing only 2 variables. The purple vertical line represents the mean correlation of Set 2, which optimizes the model results (Fig. 5).

form correlation just by fitting parameters is to generate random forces which are independent of the cyclones' positions. For this reason, the random motion is generated by randomly forcing each cyclone. This forcing is done by accelerating each cyclone with a random magnitude between -0.0017 and 0.0017 (m s^{-2}) in each direction (x and y) for consecutive periods of ~ 7 days.

Each random set, having both acceleration and position time series, goes through the same optimization procedure as presented in the previous section. Then, for each optimized set, the mean correlation is calculated by averaging the 12 correlations between the forces and accelerations of the six cyclones in the zonal and meridional directions. The resulting mean correlations of the 300 random data-sets are presented as a histogram in Fig. S3. It can be seen that the ability of the optimization to create a correlation by fitting the free variables is evaluated to be approximately 0.1, whereby using the real data, it can reach ~ 0.6 . The STD representing the Gaussian distribution of the 300 sets (Fig. S3) is ~ 0.1 , such that the probability that the mean correlation of Set 1 is a part of the random distribution is 0.0005%.

For appreciating the sensitivity of the Fig. 4 results to changes in the chosen values for the free parameters, we start with a test optimization run that has only 2 free parameters to optimize, while the other variables are pre-defined. In this test, all the cyclones are defined with the same size, velocity, and shape. The calculated forces resulting from this optimization still show a fine correlation with the acceleration data (Fig. S4 and yellow line in Fig. S3), although not as good as when the optimization had 21 free variables. In addition, a sensitivity analysis is done, where Set 1 was used as a reference for the mean correlation, and each variable is independently increased or decreased by 30% from its respective value in Set 1, while the other variables have the value from Set 1. The results of this analysis (Fig. S5) show relatively small sensitivities, as captured by the mean correlation, to changes in any one variable. The reason why some cases achieve a mean correlation higher than that of Set 1, is that the optimization does not only maximize correlation, but also tries to achieve a good match in the signs and magnitudes between the acceleration data and the forces.

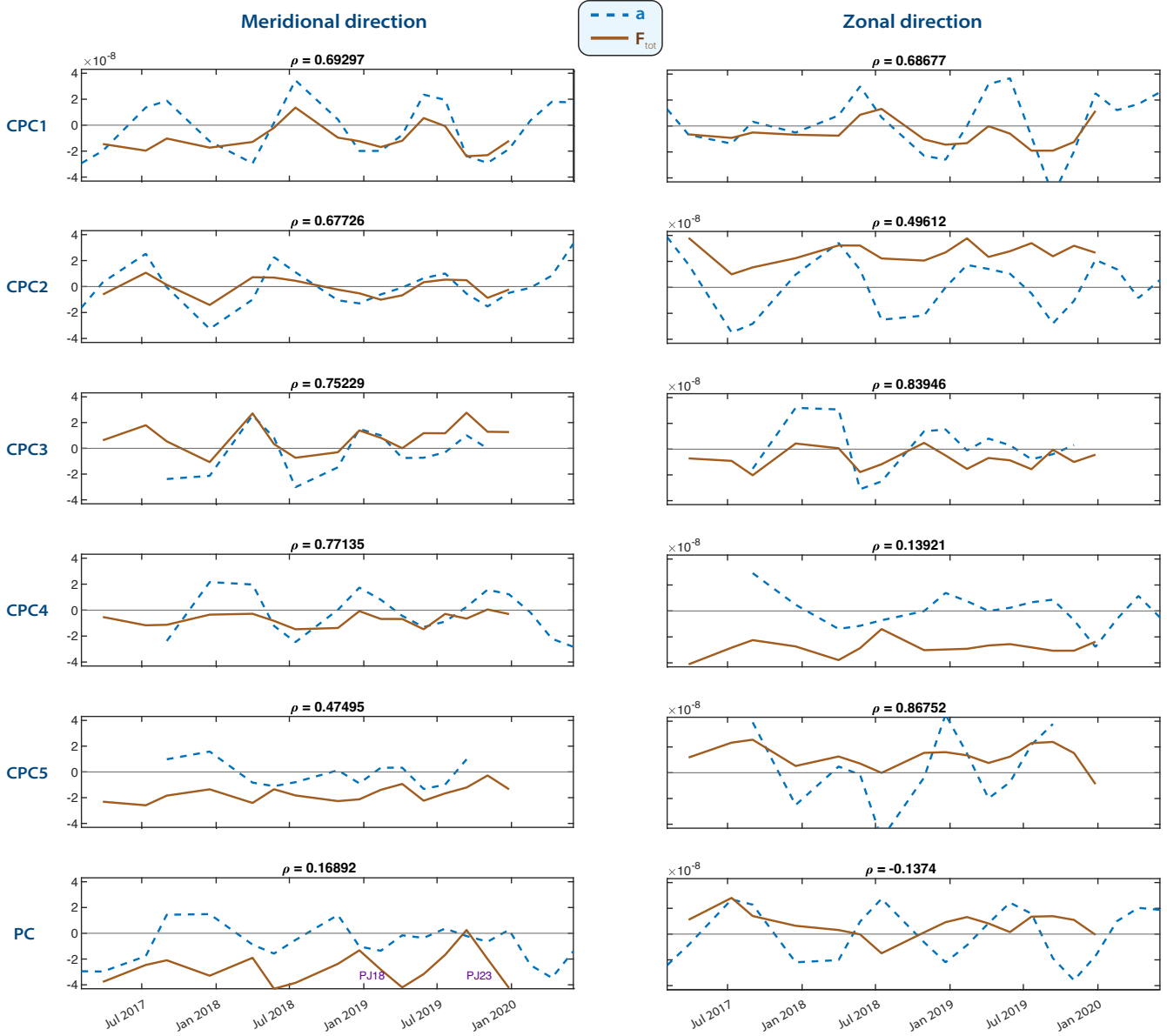


Figure S4: The same as Fig. 4, using Set 3 instead of Set 1 (Tab. S1). Here the optimization is only performed for 2 variables, where the rest of the variables are pre-defined.

C Analytic solution for the oscillations period

For finding an analytic estimate of the natural oscillation frequency, the layout of Fig. S6 is considered. The analysis is conducted on the motion of CPC2, displaced by a small x_0 from the midpoint between the adjacent CPCs 1 and 3. The neighbor CPC1 and CPC3 are assumed to be static for simplicity. Also, the cyclones are assumed to be identical. In a simple harmonic motion, the natural frequency of an oscillation pattern can be calculated by

$$\omega_N = \sqrt{\frac{k}{M}}, \quad (17)$$

where k is the spring constant and M is the mass of the cyclone. The spring constant can be calculated by a perturbation from the point of equilibrium ($x_0 = 0$) as

$$\frac{k}{M} = -\frac{\partial F}{\partial x_0}, \quad (18)$$

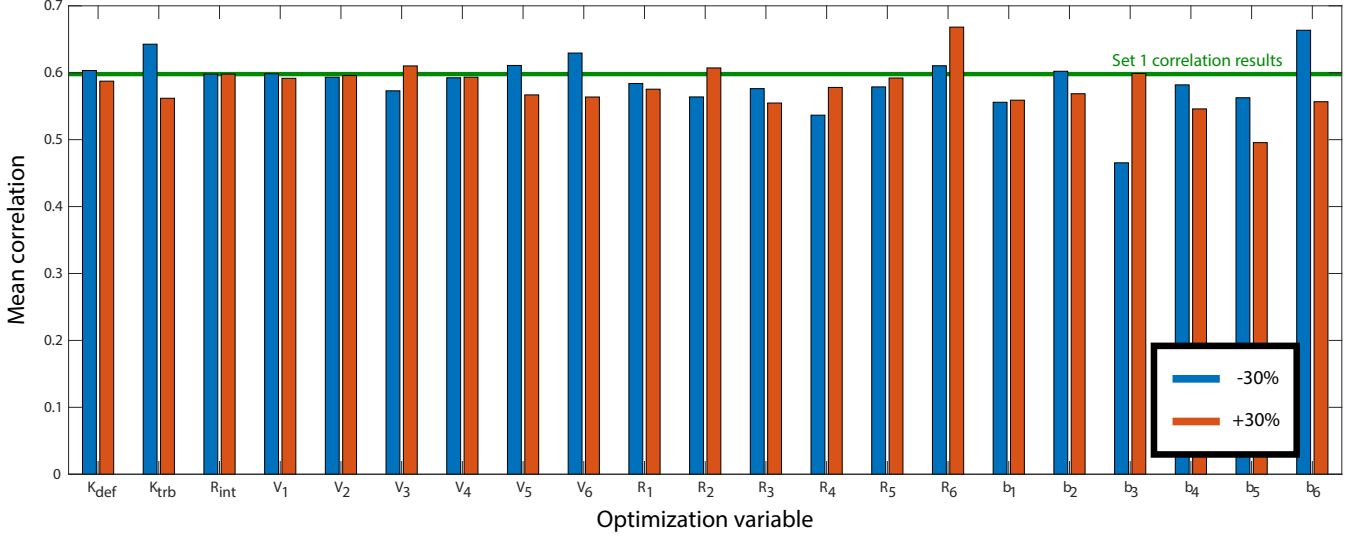


Figure S5: Sensitivity analysis for the correlation results of Fig. 4. Here, each optimized variable (Tab. S1) is decreased (blue) or increased (red) by 30%. The ordinate is the mean correlation for every test, while the horizontal green line represents the mean correlation of the optimized set.

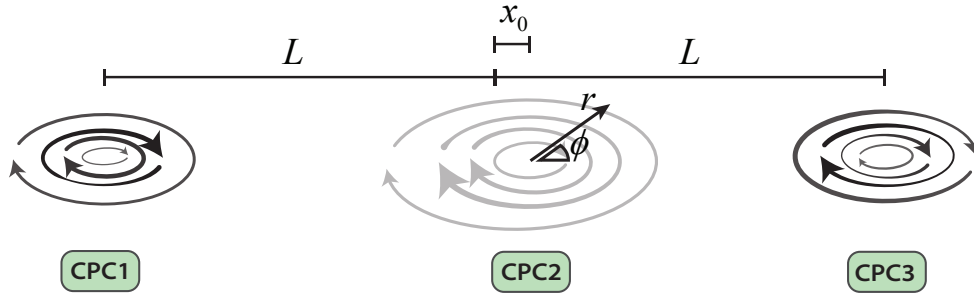


Figure S6: Schematics of the considered idealized oscillation problem. CPC1 and CPC3 are statically positioned. CPC2 is displaced by x_0 from the center between the CPCs 1 and 3, which are $2L$ apart. The polar coordinates (the radius r and angle ϕ) are defined from the center of CPC2.

where F is the mean zonal force (per unit mass) on CPC2 by the presence of CPCs 1 and 3, calculated as the integrated Coriolis force around CPC2 (for an asymptotic derivation of this force, see the Methods section in GK21),

$$F = \left(\iint dS \right)^{-1} \iint K (\xi_1 + \xi_3) v_2 dS, \quad (19)$$

where ξ_1 and ξ_3 are the vorticity contributions from CPCs 1 and 3, respectively, $K \equiv K_{\text{trb}} (1 - K_{\text{def}})$ is a constant parameterizing the effects of turbulence and meridional deflection, and v_2 is the meridional velocity field of CPC2. As the integration area ($dS = r dr d\phi$) is assumed to be within the radius of maximum velocity of CPC2, we may make the solid-rotating body approximation

$$v_2 = \frac{r}{R} V \cos \phi, \quad (20)$$

where r and ϕ represent polar coordinates around the center of CPC2, V is the maximum velocity and R is the radius of maximum velocity for the CPCs (see GK21, Extended Data Figs 1-3 for reference). The vorticity field for a CPC is estimated (see section S1) as

$$\xi_i = \frac{V}{R} \left(2 - \left(\frac{r_i}{R} \right)^b \right) \exp \left[\frac{1}{b} \left(1 - \left(\frac{r_i}{R} \right)^b \right) \right], \quad (21)$$

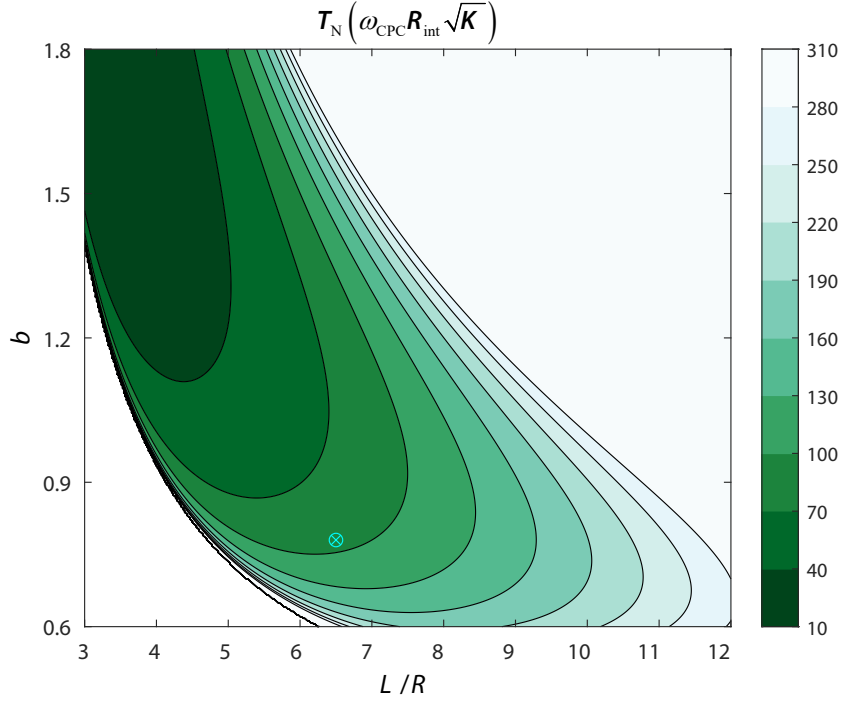


Figure S7: A contour for the values of $G = T_N(\omega_{CPC} R_{int} \sqrt{K})$. The cyan 'X' is a representative value for the south pole Jovian CPCs.

where r_i is the distance from the respective (i) CPC's core, specifically

$$\begin{aligned} r_1 &= \sqrt{(L + (x_0 + r \cos \phi))^2 + (r \sin \phi)^2} \\ r_3 &= \sqrt{(L - (x_0 + r \cos \phi))^2 + (r \sin \phi)^2} \end{aligned} \quad (22)$$

As $L \gg (x_0 + r \cos \phi; r \sin \phi)$, Eq. 22 can be approximated by

$$\begin{aligned} r_1 &= \sqrt{L^2 + 2L(x_0 + r \cos \phi)} \\ r_3 &= \sqrt{L^2 - 2L(x_0 + r \cos \phi)} \end{aligned} \quad (23)$$

As the velocity v_2 is independent of x_0 , Eq. 18 becomes

$$\frac{k}{M} = - \left(\iint dS \right)^{-1} \iint K \left(\frac{\partial \xi_1}{\partial x_0} + \frac{\partial \xi_3}{\partial x_0} \right) v_2 dS. \quad (24)$$

Using a Taylor series expansion of order $O(x_0^2)$ for ξ_i , we get

$$\left(\frac{\partial \xi_1}{\partial x_0} + \frac{\partial \xi_3}{\partial x_0} \right) v_2 \approx -e^{\frac{1}{b} \left(1 - \left(\frac{L}{R} \right)^b \right)} \frac{2\omega_{CPC}^2}{L^2} \left(\frac{L}{R} \right)^b \left(b^2 - 3b \left(\frac{L}{R} \right)^b + \left(\frac{L}{R} \right)^{2b} - 4 \right) (r \cos \phi + x_0) r \cos \phi, \quad (25)$$

where $\omega_{CPC} = \frac{V}{R}$. Then, integrating in the range $\phi = [0, 2\pi]$ and $r_i = [0, R_{int} R_i]$, Eq. 24 becomes

$$\frac{k}{M} = \frac{1}{2} \omega_{CPC}^2 R_{int}^2 K e^{\frac{1}{b} (1 - \hat{L}^b)} \hat{L}^{b-2} (b^2 - 3b\hat{L}^b + \hat{L}^{2b} - 4), \quad (26)$$

where $\hat{L} = RL$, is a normalized L . The oscillation period is thus

$$T_N = \frac{2\pi}{\omega_N} = \frac{\sqrt{8\pi}}{\omega_{CPC} R_{int} \sqrt{K}} e^{\frac{1}{2b} (\hat{L}^b - 1)} \hat{L}^{1 - \frac{b}{2}} (b^2 - 3b\hat{L}^b + \hat{L}^{2b} - 4)^{-\frac{1}{2}}. \quad (27)$$

Defining

$$G(\hat{L}, b) = \sqrt{8\pi} e^{\frac{1}{2b}(\hat{L}^b - 1)} \hat{L}^{1 - \frac{b}{2}} \left(b^2 - 3b\hat{L}^b + \hat{L}^{2b} - 4 \right)^{-\frac{1}{2}}, \quad (28)$$

we can plot how G changes with \hat{L} and with b (Fig. S7). It can be seen that for far CPCs, the oscillation period would be extremely long, where this analysis probably does not capture the leading order motion, while too small L values might lead to an instability that would break the periodic motion. For the Jovian south polar CPCs, b is ~ 0.78 and \hat{L} is ~ 6.5 , giving a value of $G \approx 100$ (cyan 'X' in Fig. S7). The cyclones' vorticity is $\omega_{\text{CPC}} \sim \frac{85}{1.1 \times 10^6}$ (sec^{-1}), while the optimization values for K_{def} , K_{trb} and R_{int} are $\sim 0.189, 0.318, 0.064$, respectively (Tab. S1, Set 1). These give T_{N} of ~ 15 months, estimating well the 12-months observed period. The remaining discrepancy might be due to the complexities of the other cyclones, their positions in space and their concurring oscillations, all of which are not taken into account in this idealized derivation.

D Oscillation model

In order to show how the underlying mechanism highlighted in this study, i.e., the mutual rejection between cyclones due to cyclone generated vorticity gradients and the cyclone polar attraction due to β , produces the observed oscillation patterns, a model is created which simulates the cyclones' motion with time according to these forces. Here, the force calculations, described in Eqs. 9-16, are used in the system of equations,

$$\begin{aligned} \frac{\partial u_i}{\partial t} &= F_{\beta i,x} + \sum_{j \neq i} F_{ji,x}, & \frac{\partial v_i}{\partial t} &= F_{\beta i,y} + \sum_{j \neq i} F_{ji,y}, \\ \frac{\partial x_i}{\partial t} &= u_{i,x}, & \frac{\partial y_i}{\partial t} &= u_{i,y}. \end{aligned} \quad (29)$$

For initial conditions, we use the first available location data, which was obtained during PJ4, as

$$x_i(0) = x_{i,\text{obs}}[\text{PJ4}], \quad y_i(0) = y_{i,\text{obs}}[\text{PJ4}], \quad (30)$$

where the subscript 'obs' refers to observational data per PJ. For the velocity initial conditions, we simply use forward derivations. For CPCs 1 and 2 and for the PC, we use

$$u_i(0) = \frac{x_{i,\text{obs}}[\text{PJ5}] - x_{i,\text{obs}}[\text{PJ4}]}{53(\text{days})}, \quad v_i(0) = \frac{y_{i,\text{obs}}[\text{PJ5}] - y_{i,\text{obs}}[\text{PJ4}]}{53(\text{days})}, \quad (31)$$

and for CPCs 3,4 and 5, where PJ5 data is missing¹, we use

$$u_i(0) = \frac{x_{i,\text{obs}}[\text{PJ6}] - x_{i,\text{obs}}[\text{PJ4}]}{106(\text{days})}, \quad v_i(0) = \frac{y_{i,\text{obs}}[\text{PJ6}] - y_{i,\text{obs}}[\text{PJ4}]}{106(\text{days})}. \quad (32)$$

From these initial conditions, the model numerically integrates Eqs. 29 over the duration of 45 months (1375 days). The integration time interval $dt = 8(\text{hrs})$ was found to be the biggest robust time step. Finally, For finding the unknown variables (i.e., K_{def} , K_{trb} , R_{int} , V_i , R_i and b_i , as defined in the text), an optimization code is performed, which minimizes the mean differences between observed and simulated values of x_i , y_i , and the mean differences between the real and the simulated motion's spectral amplitudes per period. The parameter set determined by this procedure is labeled 'Set 2' in Table. S1, and results in the simulation run shown in Fig. 5 and in movie S2. In Fig. S8, the spectra of the simulated motion is presented in terms of energy instead of metric amplitudes.

Ideal run - model robustness

For a test of the model robustness in simulating the oscillation patterns regardless of the optimization procedure, an 'ideal' model run is performed. Here, all the cyclones are identical, with $V_i = 85$ (m s^{-1}) and $R_i = 1, 100$ (km) as in GK21, and with $b_i = 0.78$. For the global coefficients, we choose $K_{\text{def}} = 0$ (no deflection), $K_{\text{trb}} = 1$ (no turbulence effect) and $R_{\text{int}} = 10\%$ (see Table. 1, 'Ideal' case for reference). For initial conditions, the cyclones started at rest ($u_i(0), v_i(0) = 0$), and are spread equally along latitude 83° , except for the PC, starting at 90° . In addition, the initial latitude of each cyclone was perturbed by a random number in the range $[-1^\circ, 1^\circ]$, and similarly in longitude by a random number in the range $[-8^\circ, 8^\circ]$. These settings produced results (Fig. S9) similar, in essence, to the observed patterns (Fig. 2), but with more dispersed spectra, as might be expected from the random initial conditions.

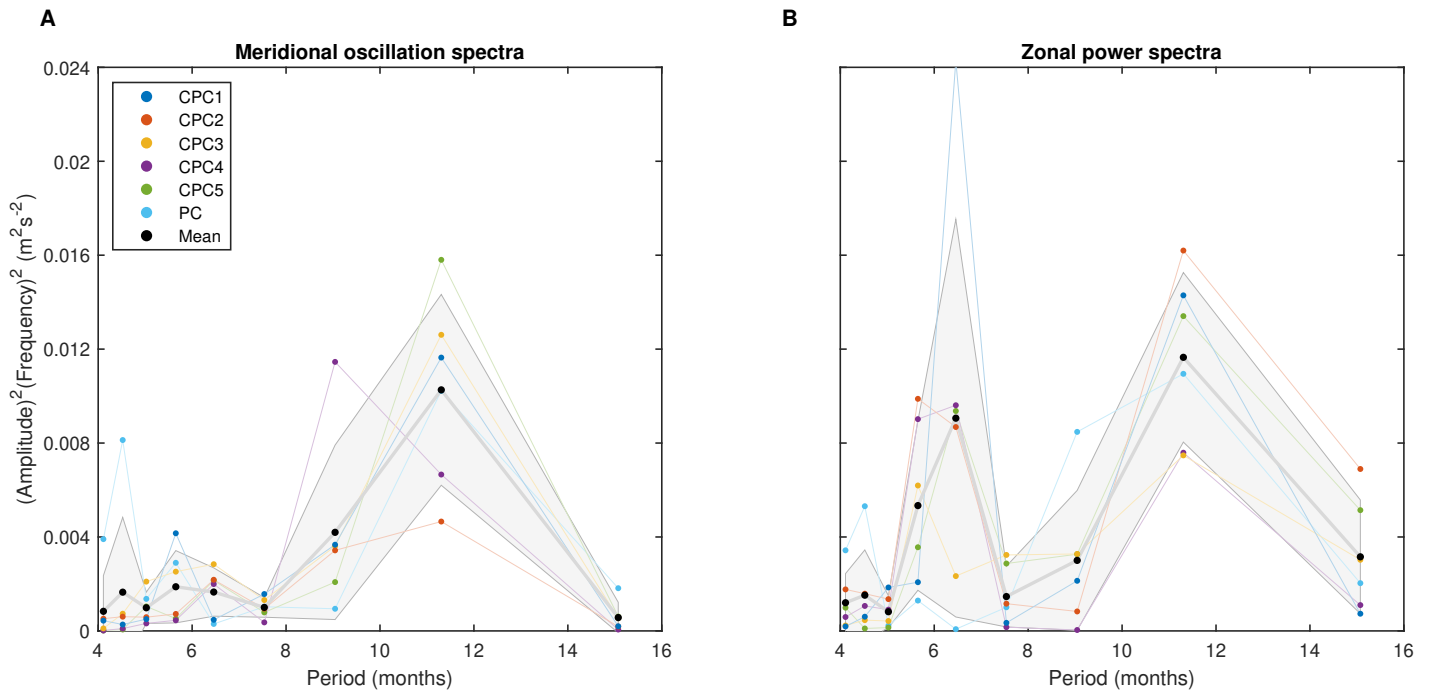


Figure S8: Energy spectra of the simulated motion. Here, panels a-b are the same as Fig. 5 panels b and c, but here the ordinate represents the energy of the oscillations ($\text{amplitude}^2 \text{ frequency}^2$) rather than just the amplitude (A_n).

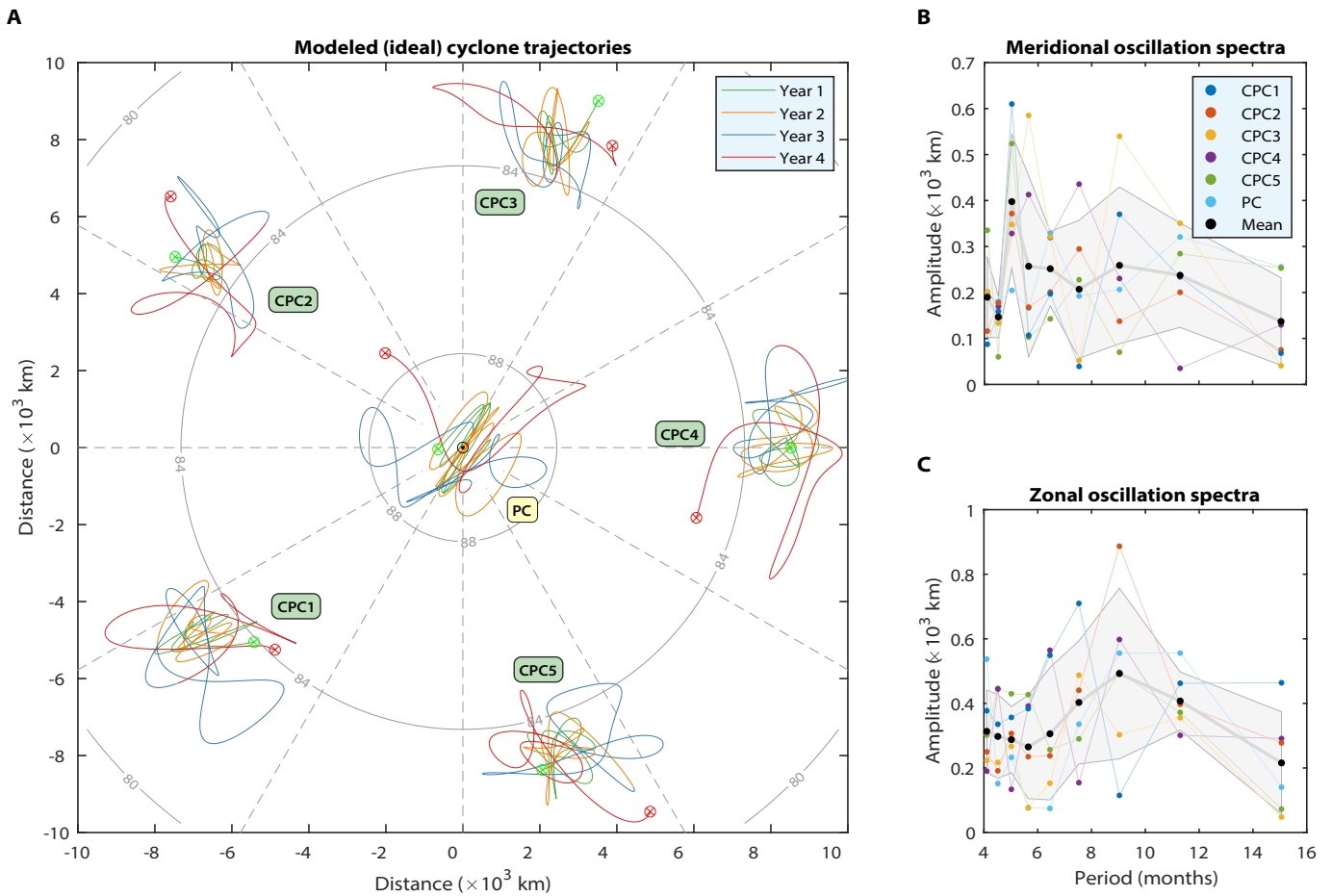


Figure S9: Ideal model simulation results. (a-c) The panels are the same as in Fig. 5. Here the cyclones are identical (Table S1, 'Ideal' case) and the initial conditions are a random perturbation from a symmetric spread.